Continuous-wave, single-pass, single-frequency second-harmonic-generation at 266 nm based on birefringent-multicrystal scheme

Kavita Devi,[1,*] S. Parsa,[1] and M. Ebrahim-Zadeh[1,2]

[1]ICFO-Institut de Ciencies Fotoniques, Barcelona Institute of Science and Technology, 08860 Castelldefels (Barcelona), Spain
[2]Institucio Catalana de Recerca i Estudis Avancats (ICREA), Passeig Lluis Companys 23, Barcelona 08010, Spain
[*]kavita.devi@icfo.es

Abstract: We report the implementation of a compact cascaded multicrystal scheme based on birefringent crystals in critical phase-matching, for the generation of continuous-wave (cw) radiation in the deep ultraviolet (UV). The approach comprises a cascade of 4 single-pass second-harmonic-generation (SHG) stages in β-BaB$_2$O$_4$ (BBO) pumped by a single-frequency cw green source at 532 nm. A deep-UV cw output power of 37.7 mW at 266 nm has been obtained with a high passive power stability of 0.12% rms over more than 4 hours. Characterization and optimization of the system in each stage has been systematically performed. Angular phase-matching acceptance bandwidth under tight focusing in BBO, and spectral properties of the deep-UV radiation, have been studied. Theoretical calculations for SHG in the cascaded scheme based on birefringent phase-matching have been performed, and enhancement in UV power compared to single-stage single-pass scheme are studied. Theoretical comparison of BBO with other potential crystals for deep-UV generation in cascaded multicrystal scheme is also presented.

References and links

1. C. Chen, T. Sasaki, R. Li, Y. Wu, Z. Lin, Y. Mori, Z. Hu, J. Wang, G. Aka, M. Yoshimura, and Y. Kaneda, *Nonlinear Optical Borate Crystals: Principals and Applications* (Wiley, 2012).
2. J. J. Ewing, "Excimer Laser Technology Development," IEEE J. Sel. Top. Quantum Electron. **6**(6), 1061–1071 (2000).
3. T. Südmeyer, Y. Imai, H. Masuda, N. Eguchi, M. Saito, and S. Kubota, "Efficient 2nd and 4th harmonic generation of a single-frequency, continuous-wave fiber amplifier," Opt. Express **16**(3), 1546–1551 (2008).
4. J. Sakuma, Y. Asakawa, and M. Obara, "Generation of 5-W deep-UV continuous-wave radiation at 266 nm by an external cavity with a CsLiB$_6$O$_{10}$ crystal," Opt. Lett. **29**(1), 92–94 (2004).
5. S. C. Kumar, K. Devi, and M. Ebrahim-Zadeh, "Stable, continuous-wave, ytterbium-fiber-based single-pass ultraviolet source using BiB$_3$O$_6$," Opt. Lett. **38**(23), 5114–5117 (2013).
6. K. Devi, S. C. Kumar, and M. Ebrahim-Zadeh, "Tunable, continuous-wave, ultraviolet source based on intracavity sum-frequency-generation in an optical parametric oscillator using BiB$_3$O$_6$," Opt. Express **21**(21), 24829–24836 (2013).
7. S. Chaitanya Kumar, J. Canals Casals, E. Sanchez Bautista, K. Devi, and M. Ebrahim-Zadeh, "Yb-fiber-laser-based, 1.8 W average power, picosecond ultraviolet source at 266 nm," Opt. Lett. **40**(10), 2397–2400 (2015).
8. L. Wang, N. Zhai, L. Liu, X. Wang, G. Wang, Y. Zhu, and C. Chen, "High-average-power 266 nm generation with a KBe$_2$BO$_3$F$_2$ prism-coupled device," Opt. Express **22**(22), 27086–27093 (2014).
9. C. Chen, S. Luo, X. Wang, G. Wang, X. Wen, H. Wu, X. Zhang, and Z. Xu, "Deep UV nonlinear optical crystal:RbBe$_2$(BO$_3$)F$_2$," J. Opt. Soc. Am. B **26**(8), 1519–1525 (2009).
10. Y. Wang, L. Wang, X. Gao, G. Wang, R. K. Li, and C. T. Chen, "Growth, characterization and the fourth harmonic generation at 266 nm of K$_2$Al$_2$B$_2$O$_7$ crystals without UV absorptions and Na impurity," J. Cryst. Growth **348**(1), 1–4 (2012).

11. S. Ilas, P. Loiseau, G. Aka, and T. Taira, "240 kW peak power at 266 nm in nonlinear $YAl_3(BO_3)_4$ single crystal," Opt. Express **22**(24), 30325–30332 (2014).
12. K. Kato, "Tunable UV Generation to 0.185 pm in CsB_3O_5," IEEE J. Quantum Electron. **31**(1), 169–171 (1995).
13. C. Chen, "Chinese lab grows new nonlinear optical borate crystal," Laser Focus World **25**(11), 129–137 (1989).
14. C. Chen, Y. Wang, B. Wu, K. Wu, W. Zeng, and L. Yu, "Design and synthesis of an ultraviolet-transparent nonlinear optical crystal $Sr_2Be_2B_2O_7$," Nature **373**(6512), 322–324 (1995).
15. Y. S. Liu, W. B. Jones, and J. P. Chernoch, "Highefficiency highpower coherent uv generation at 266 nm in 90° phase matched deuterated KDP," Appl. Phys. Lett. **29**(1), 32–34 (1976).
16. J. Reintjes and A. C. Eckardt, "Efficient harmonic generation from 532 to 266 nm in ADP and KD*P," Appl. Phys. Lett. **30**(2), 91–93 (1977).
17. S. Kurimura, M. Harada, K. Muramatsu, M. Ueda, M. Adachi, T. Yamada, and T. Ueno, "Quartz revisits nonlinear optics: twinned crystal for quasi-phase matching [Invited]," Opt. Mater. Express **1**(7), 1367–1375 (2011).
18. J. Hirohashi, T. Taniuchi, K. Imai, and Y. Furukawa, "PP-LBGO device with 2nd-order QPM structure for 266nm generation," in *Conference on Lasers and Electro-Optics Conference*, Technical Digest (OSA, 2015), paper STh3H.5.
19. K. Devi, S. C. Kumar, and M. Ebrahim-Zadeh, "13.1 W, high-beam-quality, narrow-linewidth continuous-wave fiber-based source at 970 nm," Opt. Express **19**(12), 11631–11637 (2011).
20. G. K. Samanta, S. C. Kumar, K. Devi, and M. Ebrahim-Zadeh, "Multicrystal, continuous-wave, single-pass second-harmonic generation with 56% efficiency," Opt. Lett. **35**(20), 3513–3515 (2010).
21. A. K. Hansen, M. Tawfieq, O. B. Jensen, P. E. Andersen, B. Sumpf, G. Erbert, and P. M. Petersen, "Concept for power scaling second harmonic generation using a cascade of nonlinear crystals," Opt. Express **23**(12), 15921–15934 (2015).
22. S. C. Kumar, G. K. Samanta, K. Devi, and M. Ebrahim-Zadeh, "High-efficiency, multicrystal, single-pass, continuous-wave second harmonic generation," Opt. Express **19**(12), 11152–11169 (2011).
23. R. L. Sutherland, "Frequency doubling and mixing," in *Handbook of Nonlinear Optics* (Marcel Dekker, Inc. 1996), Chap. 2.
24. D. S. Hum and M. M. Fejer, "Quasi-phasematching," C. R. Phys. **8**(2), 180–198 (2007).
25. J. E. Bjorkholm, "Optical second-harmonic generation using a focused Gaussian laser beam," Phys. Rev. **142**(1), 126–136 (1966).
26. G. D. Boyd and D. A. Kleinman, "Parametric interaction of focused Gaussian light beams," J. Appl. Phys. **39**(8), 3597–3639 (1968).
27. Y. F. Chen and Y. C. Chen, "Analytical functions for the optimization of second-harmonic generation and parametric generation by focused Gaussian beams," Appl. Phys. B **76**(6), 645–647 (2003).
28. J. M. Yarborough, J. Falk, and C. B. Hitz, "Enhancement of optical second harmonic generation by utilizing the dispersion of air," Appl. Phys. Lett. **18**(3), 70–73 (1971).
29. G. Ghosh, "Temperature dispersion of refractive indices in β-BaB_2O_4 and LiB_3O_5 crystals for nonlinear optical devices," J. Appl. Phys. **78**(11), 6752–6760 (1995).
30. D. N. Nikogosyan, *Nonlinear Optical Crystals: A Complete Survey* (Springer, 2005).

1. Introduction

Continuous-wave (cw) single-frequency sources in the ultraviolet (UV) are of great interest for many applications in science and industry including optical data storage, semiconductor wafer inspection, fiber Bragg grating fabrication, UV photolithography, holography, biomedicine, as well as absorption and fluorescence spectroscopy [1]. The predominant laser sources available in the UV region are excimer lasers, ion lasers, and free-electron lasers, with the associated limitations of non-solid-state design, bulky and complex architecture, large power comsumption, and high cost [2]. As such, an effective alternative approach for UV generation has been based on nonlinear frequency conversion techniques of second-harmonic-generation (SHG) [3,4] and sum-frequency-generation (SFG) [5,6] in suitable birefringent crystals, providing practical UV output powers.

Among the different nonlinear frequency conversion schemes, SHG of green radiation at 532 nm is the most direct approach to provide deep-UV radiation at 266 nm. To date, several nonlinear crystals have been exploited for the generation of 266 nm radiation. A list of such crystals, with transparency in the deep-UV, is shown in Table 1. For SHG to 266 nm based on critical phase-matching, β-BaB_2O_4 (BBO) offers the highest nonlinearity compared to all other birefringent crystals including $KBe_2BO_3F_2$ (KBBF), $RbBe_2BO_3F_2$ (RBBF), $K_2Al_2B_2O_7$ (KABO), $YAl_3(BO_3)_4$ (YAB) and $CsLiB_6O_{10}$ (CLBO) [7–11]. Materials such as KBBF and RBBF, while offering lower nonlinearity, are advantageous for direct SHG at wavelengths below 200 nm, as the shortest wavelength that can be generated with SHG in BBO is 205 nm.

Other nonlinear materials such as CsB_3O_5 (CBO) and LiB_3O_5 (LBO) although offer transparency below 200 nm, SHG for deep-UV generation is not feasible due to their low birefringence. As such, the lowest wavelength demonstrated with CBO and LBO are 273 nm and 277 nm, respectively [12,13]. The $Sr_2Be_2BO_7$ (SBBO) crystal with a relatively high nonlinear coefficient [14] can also be used for deep-UV generation. However, growth of this crystal is hazardous as beryllium is toxic in nature. On the other hand, temperature-tuned, zero-walk-off, noncritically phase-matched SHG at 266 nm has been demonstrated with $K(D_xH_{1-x})_2PO_4$ (DKDP) [15] and $NH_4H_2PO_4$ (ADP) [16], making these crystals potential candidates for deep-UV generation in inertial confinement fusion facilities.

With the advances in quasi-phase-matched (QPM) technology, periodically-poled crystals have been established as highly effective materials for high-power cw generation due to the high effective nonlinearity, long available interaction lengths, and absence of walk-off. At the same time, there has been a continuous quest for QPM materials providing transparency into the deep-UV. While QPM materials such as MgO-doped periodically-poled stoichiometric $LiTaO_3$ (MgO:PPsLT) provide transparency down to ~280 nm, fabrication of sufficiently short QPM gratings of high quality for UV generation still remains challenging. To date, deep-UV sources based on QPM materials have only been demonstrated in the nanosecond pulsed regime. QPM quartz has been demonstrated for 266 nm generation by performing periodic modulation of the nonlinearity by spatial patterning of a twin structure in the material [17]. Although quartz has very low nonlinearity, its very high damage threshold makes it a good candidate for high-peak-power operation. Also, very recently, pumped by a nanosecond pulsed laser, SHG at 266 nm was demonstrated in periodically-poled $LaBGeO_5$ (PP-LBGO), using 2nd-order QPM structure [18]. To exploit the highest nonlinear gain in QPM materials for SHG into the UV, 1st-order QPM grating period of $\Lambda\sim2$ μm is required, which is still challenging to fabricate. As such, 2nd order QPM structures with reduced nonlinear coefficient was used. Against this backdrop, the search for alternative birefringent and QPM materials for UV generation continues, with the most prominent candidates listed in Table 1.

Table 1. Phase-matching properties of nonlinear crystals for SHG at 266 nm[a]

	KBBF	RBBF	KABO	CLBO	BBO	YAB	DKDP	ADP	QPM quartz	PP-LBGO
θ (°)	36.3	39.9	58.1	61.6	47.6	66.9	NCPM	NCPM	NCPM	NCPM
Λ (μm)	-	-	-	-	-	-	-	-	11.9*	4.4*
$T_{crystal}$ (°C)	RT	RT	RT	140	RT	RT	60.7	51.6	RT	65
ρ (mrad)	52	56	47	32	85	33	0	0	0	0
d_{eff} (pm/V)	0.39	0.34	0.24	0.79	1.75	0.69	0.37	0.57	0.3**	0.24*

aPhase-matching angle (θ), noncritical phase-matching (NCPM), QPM grating period (Λ), crystal temperature ($T_{crystal}$), room temperature (RT), walk-off angle (ρ), and effective nonlinear coefficient (d_{eff}).
*2nd-order QPM.
**d_{eff} for SHG from 1064 nm to 532 nm.

In the cw regime, given the low pumping intensities and small nonlinear gain, only a few crystals with sufficiently high nonlinear coefficients can be considered as suitable candidates for deep-UV generation. Among these, BBO, offering the highest nonlinear coefficient of all birefringent crystals for UV generation, has been used for maximum cw power generation at 266 nm [3]. Another competitive material for UV generation at this wavelength is CLBO. With a lower spatial walk-off than BBO, CLBO has also been demonstrated to provide high cw output powers [4]. To enhance the nonlinear gain, and thus the cw output power using these nonlinear materials, the common approach has been to deploy the well-established external enhancement cavities. Although such configurations result in high output powers, to minimize output power fluctuations, even to ~1% rms, frequency locking of the enhancement cavities using techniques such as Pound-Drever-Hall are imperative, which inevitably lead to

increased size and complexity. On the other hand, single-pass schemes are simple, compact and robust [19]. Moreover, they enable direct transfer of frequency and power stability of the input to the frequency-converted output beam without the need of active stabilization. However, due to the low nonlinear coefficient of the available materials in the deep-UV (see Table 1), the single-pass SHG scheme generally results in low cw output powers. To enhance output power and efficiency in the single-pass scheme, we previously reported an effective alternative technique based on a three-stage multicrystal cascaded scheme using the QPM nonlinear material of MgO:PPsLT, enabling major enhancement in single-pass cw SHG efficiency and output power at 532 nm [20]. Also recently, two-crystal cascade configurations were demonstrated for power enhancement together with efficient thermal handling, where the first crystal provided the high nonlinear efficiency, and the subsequent crystal was chosen for power handling capability [21]. For the attainment of cw power enhancement in the deep-UV in a simple and compact design, while maintaining high output power stability, it is thus highly desirable and timely to extend and study the multicrystal cascaded single-pass SHG scheme in birefringent crystals for UV generation. Here, we investigate this technique and study the SHG enhancement factor in birefringent material in presence of spatial walk-off under critical phase-matching. We use a cascaded single-pass scheme comprising 4 stages, and investigate the system performance, for the first time. As BBO is still the most well-established birefringent material for deep-UV generation, offering the highest effective nonlinearity and most competitive performance, with widespread commercial availability, we choose this crystal for the present study. The birefringent-multicrystal (B-MC) scheme used in this work permits independent focusing, mode matching, and angular tuning in each SHG stage. The technique also allows the use of several shorter crystals in cascade, which is advantageous when deploying nonlinear crystals with large spatial walk-off. Using the scheme, we have generated multi-tens of mW of output power at 266 nm, with a high passive power stability of 0.12% rms over more than 4 hours. For many aforementioned applications that demand precise high-resolution measurements, such a simple compact UV source, with practical powers, single-frequency output, and high power stability are primary requirements.

2. Experimental setup

The schematic of the experimental setup for single-pass SHG in B-MC scheme is shown in Fig. 1. The fundamental source is a cw single-frequency solid-state laser (Coherent, Verdi 10), delivering up to 10 W of output power at 532 nm in a linearly polarized beam with $M^2<1.1$. The input power to the SHG crystals is adjusted by using a combination of half-wave plate and a polarizing beam-splitter cube. A second half-wave plate is used to obtain the required polarization for phase-matching in the SHG crystals.

The setup comprises of four single-pass SHG stages, with each stage comprising BBO as the nonlinear crystal. The crystals are all cut at $\theta = 47.56°$ for type I ($oo \rightarrow e$) critically phase-matched SHG to 266 nm. We used three identical crystals, each 10-mm-long in stage-1, 2, and 3, and one 5-mm-long BBO crystal in stage-4. The end-faces of the crystals are antireflection-coated ($R<0.1\%$) at 532 and 266 nm. Optimum phase-matching for SHG is achieved by angular rotation of BBO crystals in each stage at room temperature. Using a lens, L, the green fundamental beam at 532 nm is focused at the center of the BBO crystal in stage-1, generating SHG output at 266 nm. In stage-2, the generated SHG output and the unconverted fundamental after stage-1 are collimated and refocussed at the centre of the BBO crystal using plano-concave mirrors, M_1 and M_2. The SHG output thus generated, together with the undepleted fundamental after stage-2, are again collimated and refocused at the centre of the BBO crystal in stage-3, using mirrors, M_3 and M_4, and finally focused into the BBO crystal in stage-4, using mirrors, M_5 and M_6. The focal length (f) of lens, L, and of all the mirrors, M_1-M_6, are chosen to achieve the required beam waist for mode-matching, and optimum performance of the system, as listed in Table 2. All plano-concave mirrors are coated for high reflectivity ($R>99\%$) at 532 nm and 266 nm. To adjust the inter-crystal

spacing, to compensate any accumulated phase in the interacting waves due to dispersion in air [22], the crystals and mirrors are mounted on translation stages. The generated UV output is
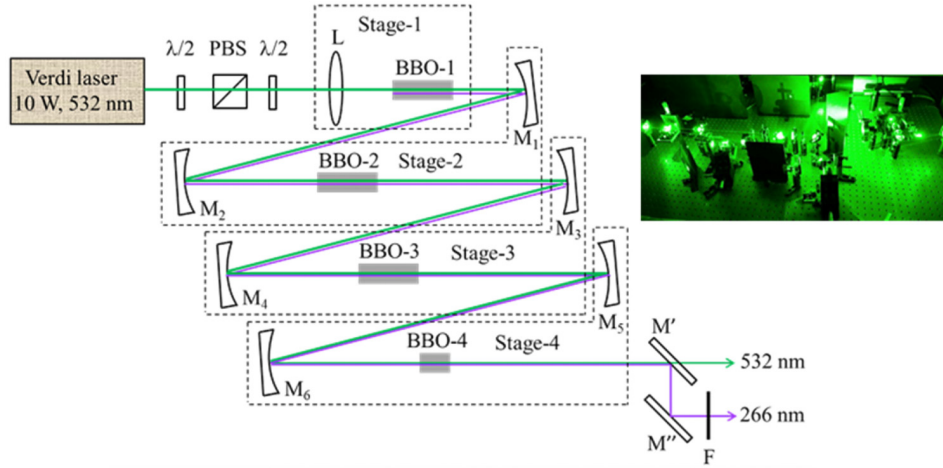

Fig. 1. Schematic of the B-MC single-pass SHG. PBS: Polarizing beam-splitter; L: lens; M_1-M_6: Mirrors; M', M": Dichroic mirror; F: Filter. Inset(right-hand): Photograph of the experimental setup.

separated from the fundamental by using an identical pair of dichroic mirrors, M' and M" ($T>98\%@532$ nm, $R>99\%@266$ nm). To further reject any residual fundamental from the UV, an additional filter, F (FGUV5, $T>79\%@266$ nm), is used. Inset of Fig. 1 shows the photograph of the laboratory experimental setup.

Table 2. Collimation and focussing optics used in each SHG stage

	Stage-1	Stage-2		Stage-3		Stage-4	
Optical elements	L	M_1	M_2	M_3	M_4	M_5	M_6
f (mm)	150	100	75	50	50	75	100
Beam waist (µm)	29	19		16.5		22	

3. UV power and efficiency

3.1 Theory

For the attainment of efficient SHG in birefringent crystals under critical phase-matching at room temperature, optimum focusing of the fundamental beam within the crystal is critical. Due to the spatial walk-off in birefringent crystals, the interacting waves maintain spatial overlap only for a limited length in the medium. This effective length is given by [23],

$$l_{eff} = \frac{\sqrt{\pi} w_F}{\rho},\qquad(1)$$

where w_F is the fundamental beam waist radius and ρ is the walk-off angle between the second-harmonic and fundamental beam.

The SHG output power, under the plane-wave approximation with no pump depletion, is given by [23],

$$P_{2\omega} = \frac{8\pi d_{eff}^2}{n_\omega^2 n_{2\omega} c \varepsilon_0 \lambda_\omega^2} \left(\frac{P_\omega^2 l^2}{w_F^2} \right) \sin c^2 \left(\frac{\Delta k l}{2} \right),\qquad(2)$$

where d_{eff} is the effective nonlinear coefficient, P_ω is the fundamental power, l is the crystal physical length, Δk is the phase-mismatch, n_ω and $n_{2\omega}$ are the refractive indices of the fundamental and SHG beam, respectively, and λ_ω is the fundamental wavelength. Under focused Gaussian beam condition, the SHG power is given by [24,25],

$$P_{2\omega} = \frac{16\pi^2 d_{eff}^2 h(B,\xi) P_\omega^2 l}{n_\omega n_{2\omega} c \varepsilon_0 \lambda_\omega^3},$$ (3)

where $h(B,\xi)$ is the nonlinear coupling coefficient [26,27], and B is the walk-off parameter given by [26],

$$B = \frac{\rho \sqrt{(l k_\omega)}}{2},$$ (4)

and ξ is the focusing parameter given by [26],

$$\xi = \frac{l}{k_\omega w_F^2},$$ (5)

where k_ω is the fundamental wavevector in the crystal.

Thus, for birefringent crystals, under loose focusing, when walk-off effects are negligible, and when $l \ll l_{eff}$ and $l \ll z_R$ ($z_R = \pi w_F^2/\lambda_\omega$ is the Rayleigh range), the SHG power is given by Eq. (2), and [25],

$$P_{2\omega} \propto \frac{l^2}{w_F^2}$$ (6)

However, under tight focusing, when walk-off effects are prominent and $l_{eff} \ll l \ll z_R$, Eq. (3)_ comes into effect, so that [25]

$$P_{2\omega} \propto \frac{\sqrt{\pi} l}{w_F \rho}.$$ (7)

3.2 Single-crystal

In order to characterize the single-pass SHG scheme and optimize the focusing condition, we first performed power scaling measurements with both 10-mm-long and 5-mm-long BBO crystals in the single-crystal (SC) scheme. The single-pass SHG with 10-mm-long BBO in SC scheme was achieved by focusing the fundamental beam at the centre of the crystal, using lenses, *L*, of different focal lengths. Initially, we focused the fundamental to a beam waist radius of $w_F = 21$ μm, for which a maximum UV power of 12.07 mW was achieved for 9.2 W of fundamental power. With the fundamental beam loosely focused to a beam waist radius of $w_F = 29$ μm, a UV power of 12.28 mW was obtained. With further increase in the beam waist to $w_F = 32.5$ μm, a drop in the SHG power down to 6.03 mW was observed. As expected, the SHG cw output powers are low in the single-pass scheme. Since the change in the SHG output power for beam waist below $w_F = 29$ μm is not significant, we fixed the fundamental waist at $w_F = 29$ μm, and performed power and efficiency scaling measurements. The results are shown in Fig. 2(a). As can be seen, the SHG power increases quadratically, with a linear increase in the corresponding SHG efficiency, up to the maximum fundamental power of 9.2 W, thus indicating the absence of pump depletion and thermal effects at these power levels. Considering a calculated spatial walk-off angle of $\rho = 85$ mrad, and a fundamental beam waist of $w_F = 29$ μm, the effective length of the crystal is calculated to be $l_{eff} = 0.6$ mm.

Using a crystal of shorter length, 5 mm, we then characterized the single-pass SC scheme for UV generation. We focused the fundamental beam to different beam waist radii of $w_F =$

14, 21, and 29 μm at the centre of the crystal, and obtained UV ouput powers of 7.3 mW, 8.8 mW and 7.2 mW, respectively, at the maximum fundamental power of 9.2 W. Keeping the beam waist fixed at w_F = 21 μm, as shown in Fig. 2(b), we performed power and efficiency scaling measurements, where again the SHG power shows quadratic dependence, and efficiency shows linear dependence, on the fundamental power.
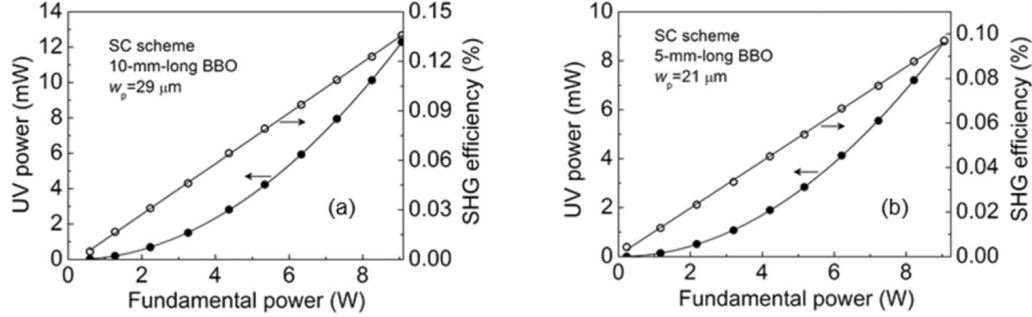

Fig. 2. Variation of UV power and SHG efficiency as a function of fundamental power in SC scheme with (a) 10-mm-long, and (b) 5-mm-long BBO.

3.3 Multicrystal

To investigate the performance of the B-MC scheme, we characterized the system and studied the enhancement in output SHG power and efficiency after each stage. We recorded the SHG power and efficiency as a function of fundamental power in 2-crystal, 3-crystal, and 4-crystal configurations. The power and efficiency scaling measurements after each stage are shown in Figs. 3(a) and 3(b), respectively. The fundamental power is measured before stage-1, while the UV power is measured after separation from the fundamental after each stage. The 2-crystal configuration is realized with two 10-mm-long BBO crystals in the cascade, leading to a total
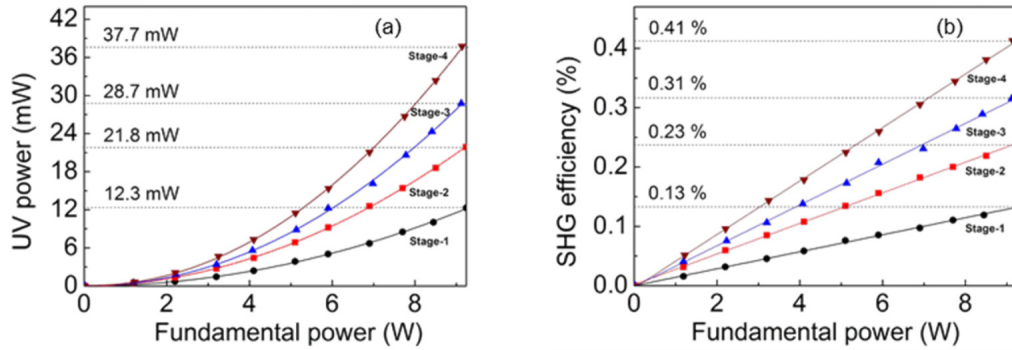

Fig. 3. (a) UV power, and (b) SHG efficiency versus fundamental power after each stage in B-MC scheme.

physical crystal length of 20 mm. The SHG output and the undepleted fundamental from stage-1 are collimated and focussed into the second identical BBO crystal in stage-2. Given the higher SHG power obtained with beam waists at or smaller than w_F = 29 μm for the 10-mm-long crystal in the single-pass scheme, the beam waist at the centre of the crystal in stage-2 was chosen to be w_F~19 μm, leading to a total effective length, l_{eff} = 0.99 mm. The 3-crystal configuration was realized by collimating and focusing the SHG output and the unconverted fundamental from stage-2, into a third identical 10-mm-long BBO crystal in stage-3. The total physical length of the crystal in stage-3 was 30 mm. The beam waist used

for SHG in stage-3 was w_F = 16.5 μm, resulting in an increase in the total effective length to l_{eff} = 1.33 mm. We further collimated and focused the SHG output and the residual fundamental from stage-3 into a fourth BBO crystal of 5-mm length in stage-4. The total physical length of the crystal at stage-4 was now 35 mm. As the optimum beam waist obtained for 5-mm-long BBO in SC scheme was w_F = 21 μm, we chose the beam waist at the centre of the crystal in stage-4 to be w_F~22 μm. This resulted in a total effective length of l_{eff} = 1.79 mm at stage-4. As evident, the beam waist (w_F = 16.5 μm) used in stage-3 is smaller than that used in stage-1 and 2. With the increase in the beam waist in stage-3, while using focal length of 75 mm for mirror M_4, a drop in the total UV output power was observed. Also, unlike the multicrystal scheme using QPM
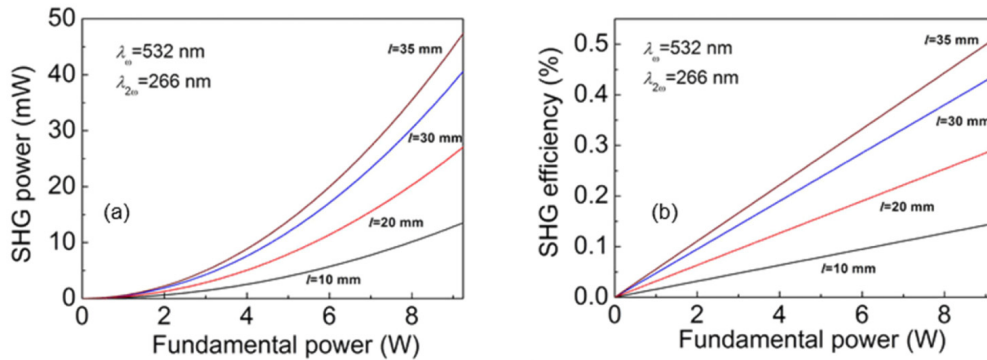

Fig. 4. (a) Theoretical UV power and (b) SHG efficiency scaling for different crystal lengths in B-MC scheme.

materials [20], here in the B-MC scheme, given the absence of thermal loading in the crystals, the beam waist at the centre of each crystal is chosen for maximum SHG efficiency. Considering the walk-off compensation possibility in the B-MC scheme, the orientation of the crystal in the successive stages was always adjusted for the maximum UV power generation. At the same time, to compensate for any possible phase shifts between the interacting waves due to the dispersion in the air, the distance between the crystals is always adjusted for maximum SHG power, as described previously for doubling into the green [22]. However, it should be noted that the phase shift arising from the increased dispersion in air is larger for SHG into the deep-UV as compared with doubling into the green. This means that the change in the mirror position resulting in a total phase shift of a multiple of 2π between the fundamental green and the second-harmonic deep-UV after reflection from the mirrors is smaller for deep-UV generation [28]. Moreover, since in the B-MC scheme, phase-matching is attained by independent angular rotation of the crystal at each stage, this provides an additional means to compensate for any phase shift due to dispersion in air. As can be seen in Fig. 3(a), after each stage, the SHG power increases quadratically, and, as evident in Fig. 3(b), the SHG efficiency rises linearly up to the maximum fundamental power of 9.2 W. We achieved maximum UV power of 12.3 mW, 21.8 mW, 28.7 mW, and 37.7 mW, with corresponding efficiency of 0.13%, 0.23%, 0.31% and 0.41%, after stage-1, 2, 3 and 4, respectively, at 9.2 W of input power. The linear variation of efficiency with the input power indicates the absence of thermal effects even in the 4-crystal configuration.

We have further performed theoretical calculations for SHG power and efficiency, as a function of incident fundamental power for BBO of lengths 10 mm, 20 mm, 30 mm and 35 mm, as shown in Figs. 4(a) and 4(b). The calculations are performed under tight focussing conditions, with no pump depletion, no thermal effects and negligible loss, using relevent Sellmeier equations for the material [29]. Here, the non-zero SHG input at successive stages is considered by increasing the length of the crystals at each stage. As can be seen, Figs. 3(a)

and 3(b) follow exactly the same behavior as in Figs. 4(a) and 4(b), respectively, confirming good agreement between the experimental data and calculations.

Since, under tight focusing conditions, the calculated total effective length is much smaller than the crystal physical length, the SHG power scales linearly with the length of the nonlinear crystal. Figure 5(a) shows the generated UV power as a function of crystal length. As evident, the SHG power shows linear dependence on the length of the nonlinear crystal
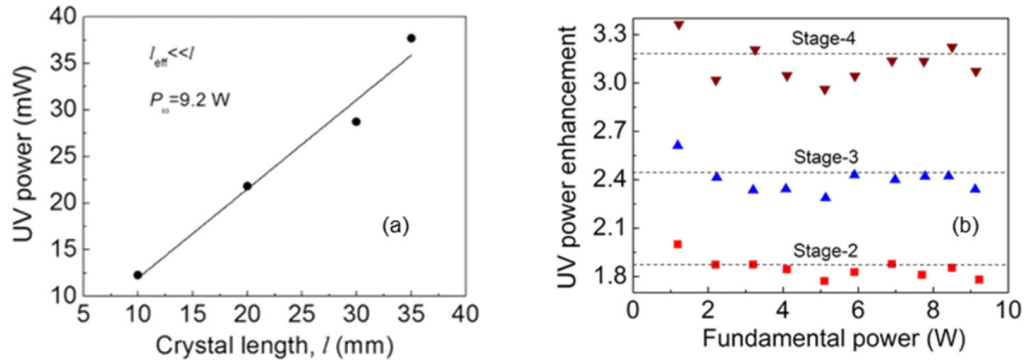

Fig. 5. (a) Variation of UV power as a function of crystal length under tight focusing at maximum fundamental power. (b) SHG power enhancement factor as a function of fundamental power at different stages in B-MC scheme.

used in each stage. We further studied the SHG power enhancement factor in B-MC scheme by determining the ratio of the UV power after each stage to that of after stage-1, as a function of fundamental power. The results are shown in Fig. 5(b). The SHG power enhances by a factor of 1.88, 2.45, and 3.18 in stage-2, stage-3, and stage-4, respectively. The slight discrepancy from the theoretical enhancement in SHG power in each stage is due to the non-identical optimum beam waists at different stages, and also could be due to the losses in mirror and crystal coatings, which could be significant at these power levels.

4. Theoretical comparison with other crystals

Among the different birefringent crystals for deep-UV generation listed in Table 1, CLBO has the next lower nonlinear coefficient and spatial walk-off angle than BBO. We, thus, theoretically compare the performance of BBO with CLBO in B-MC scheme. Also, we compare the performance with QPM crystal, PP-LBGO, where the absence of spatial walk-off, despite the reduced effective nonlinearity due to higher-order quasi-phase-matching, could potentially enhance SHG efficiency and output power. Figure 6(a) shows the calculated $h(B,\xi)$ as a function of ξ, according to Boyd and Kleinman theory [26,27], for BBO, CLBO and PP-LBGO, for crystal length of 10 mm each. Considering $\rho = 85$ mrad for the BBO crystal, corresponding to a walk-off parameter of $B\sim18.9$, the maximum nonlinear coupling coefficient of $h(B,\xi)\sim0.037$ is obtained for $\xi = 1.4$. Similarlly, for the CLBO crystal, with a walk-off angle of $\rho = 31.4$ mrad, corresponding to a walk-off parameter of $B\sim6.6$, we obtain a maximum $h(B,\xi)\sim0.107$ for $\xi = 1.41$. The zero spatial walk-off in PP-LBGO leads to $B = 0$, and thus a maximum nonlinear coupling coefficient of $h(B,\xi) = 1.067$ is obtained for $\xi = 2.8$. Using the maximum $h(B,\xi)$ and thus the corresponding fundamental beam waists of $w_F = 19$ μm (BBO), $w_F = 20$ μm (CLBO) and $w_F = 13$ μm (PP-LBGO), for efficient SHG in each crystal
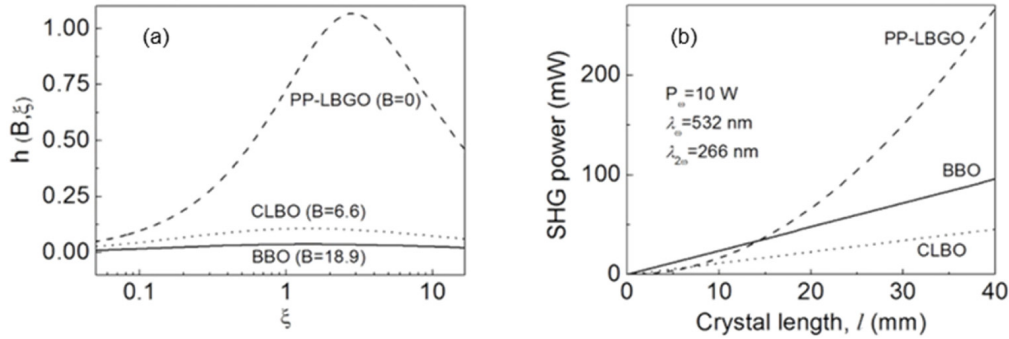
Fig. 6. (a) Variation of the calculated nonlinear coupling coefficient, $h(B,\xi)$, as a function of focusing parameter, ξ, in different crystals. (b) Theoretical SHG power as a function of crystal length for 10-mm-long crystals in cascade in B-MC scheme for different crystals.

type, we calculated the SHG output power as a function of crystal length for 10-mm-long crystals in cascade for multicrystal configuration. The results are shown in Fig. 6(b), where the relevent Sellmeier equations have been used for the crystals [29,30], and the fundamental power of $P_\omega = 10$ W at 532 nm has been used for calculations. Again, the calculations are performed with no pump depletion, no thermal effects and negligible loss approximation. As evident, despite the smaller walk-off angle in CLBO, the SHG output powers obtained are not higher than BBO. On the other hand, with second-order quasi-phase-matching in PP-LBGO, significantly higher SHG powers than BBO can be obtained with increasing crystal lengths above ~15 mm, due to NCPM in the absence of spatial walkoff. However, the challenge with QPM materials for deep-UV generation still remains their fabrication in large scale and long interaction lengths. The performance of multicrystal single-pass configuration for BBO, CLBO and PP-LBGO are compared and summarized in Table 3.

Table 3. Comparision of different crystals for single-pass SHG in multicrystal configuration

	B	ξ	$h(B,\xi)$	l (mm)	$P_{2\omega}$ (mW)	$\eta_{2\omega} = P_{2\omega}/P_\omega$ (%)
BBO	18.9	1.4	0.037	40	95	0.95
CLBO	6.6	1.41	0.107	40	46	0.46
PP-LBGO	0	2.8	1.067	40	267	2.67

5. Power stability

We characterized and compared the performance of the deep-UV source for power stability under SC and B-MC scheme. Figure 7(a) and 7(b) show the recorded passive power stability of the generated UV in the SC scheme with the 10-mm-long BBO and 5-mm-long BBO, respectively, at the maximum fundamental power of 9.2 W, under free-running conditions. The UV power is recorded to exhibit passive stability better than 0.1% rms for the 10-mm-long BBO, and 0.12% rms for the 5-mm-long BBO, over 2 hours. To compare the power stability of the UV output to the input fundamental in the single-pass scheme, we also recorded the passive power stability of the fundamental at maximum power. The result is shown in Fig. 7(c). The power stabilities in Figs. 7(a) and 7(b) are identical to the passive power stability of 0.1% rms over 2 hours for the fundamental in Fig. 7(c). As evident, the stability in power is directly transferred from the input fundamental to the UV output in the single-pass scheme. Figure 7(d) shows the long-term passive power stability of the UV output in B-MC scheme after stage-4, at maximum fundamental power of 9.2 W. The UV output after stage-4 is recorded to exhibit a passive power stability better than 0.12% rms over more than 4 hours. It is evident that the addition of crystals in single-pass cascaded scheme does not result in any additional instabilities in the UV output power. Moreover, we have not

observed any sign of power degradation or optical damage to any of the crystals or the coatings in B-MC scheme, under long-term operation.
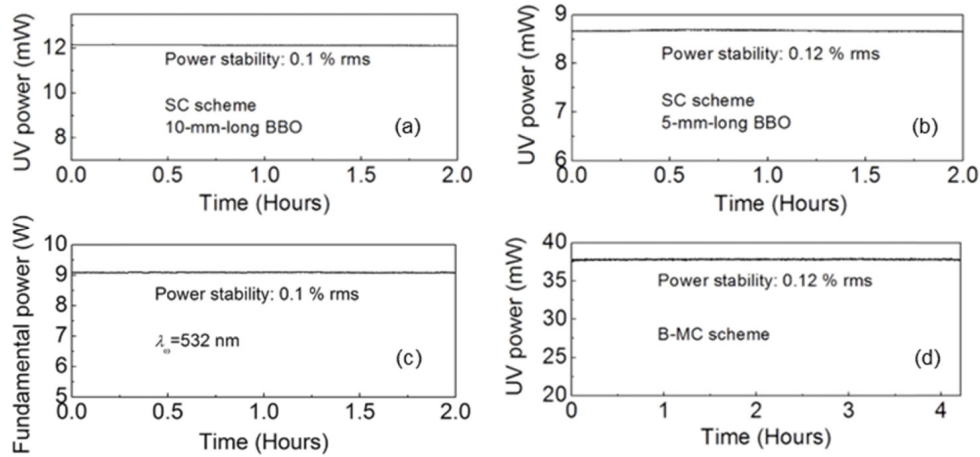

Fig. 7. Passive power stability of the UV output in the SC scheme for (a) 10-mm-long BBO, and (b) 5-mm-long BBO. (c) Fundamental power stability. (d) Passive power stability of the UV output in B-MC scheme after stage-4.

6. Angular acceptance bandwidth

We also studied the angular acceptance bandwidth of the 5-mm-long BBO crystal for SHG at room temperature by measuring the variation of the UV output power as a function of crystal
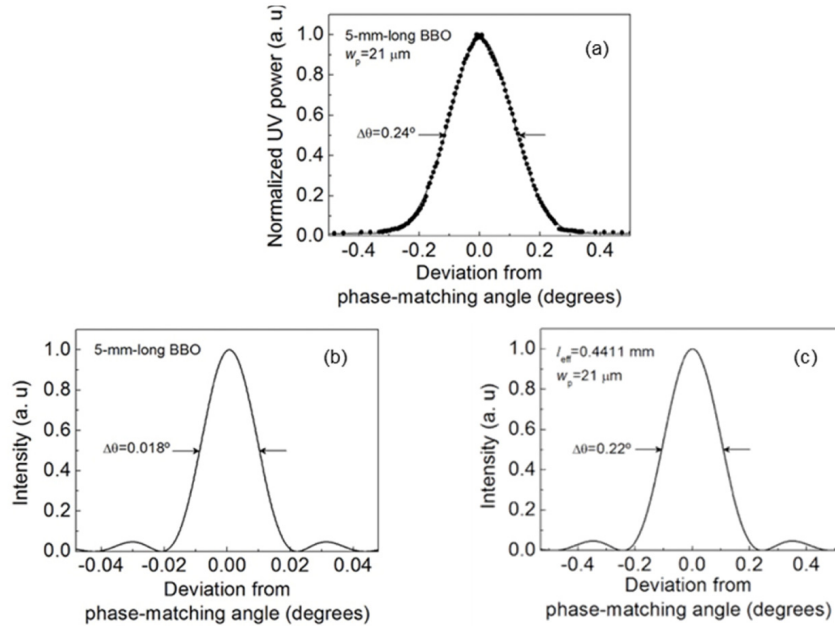
Fig. 8. (a) Experimentally measured, and (b) theoretically calculated angular acceptance bandwidth of UV output for a 5-mm-long BBO crystal. (c) Theoretically calculated angular acceptance bandwidth for an effective length of $l_{eff} = 0.44$ mm.

angle, θ, at a low fundamental power of 3.7 W. We used a fundamental beam waist of $w_F = 21$ μm for maximum SHG efficiency. The angular acceptance profile obtained is shown in

Fig. 8(a). The experimental data has a full-width at half-maximum (FWHM) bandwidth of $\Delta\theta$ = 0.24°. Figure 8(b) shows the corresponding theoretical angular acceptance curve calculated using the relevant Sellmeier equations for BBO [29], where a FWHM bandwidth of $\Delta\theta$ = 0.018°, at a phase-matching angle of θ = 47.56°, is obtained. The large difference in the experimental and calculated angular acceptance bandwidth is attributed to the presence of large spatial walk-off effect in BBO under tight focussing. Using a effective length of l_{eff} = 0.44 mm corresponding to the beam waist of w_F = 21 μm used in BBO, we obtain a theoretical FWHM bandwidth of $\Delta\theta$ = 0.22°, as shown in Fig. 8(c), which is in close agreement with the measured bandwidth in Fig. 8(a).

7. Spectrum and beam quality

To investigate the single-frequency operation of the generated UV in B-MC scheme, the spectral characteristics of the UV beam after stage-4 and the fundamental were studied. Figure 9(a) shows the spectrum of the generated UV output, measured simultaneously with the green fundamental, using a spectrometer with a resolution of 0.27 nm (OceanOptics, HR4000), at central wavelength of 266 nm and 532 nm, respectively. Given the lack of suitable optics at
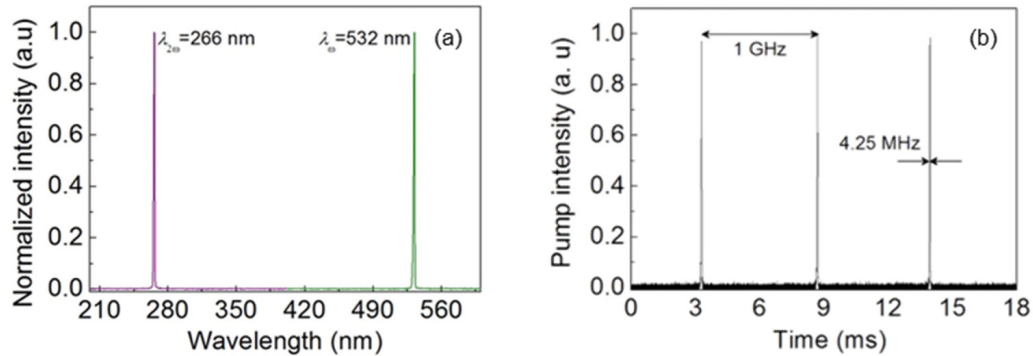

Fig. 9. (a) Spectrum of the SHG output and the input fundamental. (b) Single-frequency spectrum of fundamental measured at maximum power operation.

266 nm for a Fabry-Perot interferometer (FPI), we were not able to detect the transmission spectrum of the UV. However, we measured the spectrum of the fundamental using a confocal FPI (FSR = 1 GHz, finesse = 400), confirming single-frequency emission with an instantaneous linewidth of 4.25 MHz, as shown in Fig. 9(b). Given the single-pass SHG scheme used here, it is thus expected that the UV output is also single-frequency. Using energy conservation (Manley-Rowe relations) between the fundamental and the second-harmonic output, the bandwidth of the UV output has been calculated to be 8.5 MHz.

We also characterized the near-field energy distribution of the UV output in SC and B-MC scheme. Figure 10(a) shows the UV beam profile together with the orthogonal intensity distributions at maximum power in the SC scheme with 10-mm-long BBO crystal. As can be seen, the UV output beam is highly elliptic with a circularity of only ~5% due to the large spatial walk-off in BBO. However, the beam can be readily circularized using suitable cylindrical optics [7]. Given the large spatial walk-off in each crystal in the B-MC scheme, the UV output after stage-4 is also elliptic and requires focusing optics to collect the beam on the camera. Using a lens, we recorded the near-field energy distribution of the UV output after stage-4, at maximum fundamental power, as shown in Fig. 10(b). As can be seen, we were able to greatly improve the spatial profile of the UV beam, resulting in a Gaussian profile with circularity of >70%.
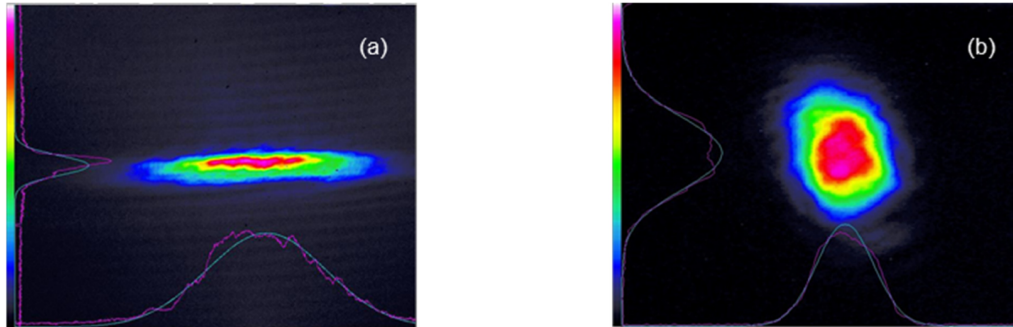
Fig. 10. Near-field energy distribution of UV output in (a) SC scheme with 10-mm-long BBO, and (b) B-MC scheme after stage-4 using focussing lens.

8. Conclusions

We have demonstrated and studied single-pass multicrystal SHG scheme for the generation of cw deep-UV radiation at 266 nm using the birefringent crystal of BBO. Using fundamental cw single-frequency radiation at 532 nm, and four BBO crystals in a cascade, we have achieved ~38 mW of output power at 266 nm, with a passive power stability of 0.12% rms over 4 hours in Gaussian spatial beam quality with a circularity of >70%. The linear nature of SHG efficiency power scaling suggests that by using higher fundamental powers and larger number of widely available BBO crystals in cascade, the cw single-pass SHG power and efficiency in the deep-UV can further be increased. In addition, techniques such as elliptical focusing and double-crystal walk-off compensation in each conversion stage could also be potentially deployed in the B-MC scheme to enhance the overall SHG output power and efficiency into the deep-UV. The theoretical calculations performed to study the performance of other potential crystals for deep-UV generation in multicrystal scheme also suggest the possibility of increase in UV power at 266 nm by using QPM materials. Such simple, compact, single-frequency and low-noise deep-UV source, with practical powers, good spatial beam quality, and excellent power stability paves the way for many applications including biomedicine and spectroscopy that demand precise high-resolution measurements.